

Robust inertial sensing with atom interferometry in the signal regime of partial interference fringes

Yun-Jhih Chen^{2,3,*}, Azure Hansen¹, Moshe Shuker¹, Rodolphe Boudot^{1,4}, John Kitching¹, and Elizabeth A. Donley¹

¹Time and Frequency Division, National Institute of Standards and Technology, Boulder, Colorado 80305, USA

²Associate of the National Institute of Standards and Technology, Boulder, Colorado 80305, USA

³Department of Physics, University of Colorado, Boulder, Colorado 80309, USA and

⁴FEMTO-ST, CNRS, 26 rue de l'Épitaphe 25030 Besançon, France

Point source atom interferometry (PSI) measures one axis of acceleration and two axes of rotations from interferometer fringe images. The data acquisition and image analysis typically rely on the number of fringes in the image, which is proportional to the rotation rate. We introduce a new method for PSI-based rotation measurement, which is effective in both the multiple-fringe regime and the notorious partial-fringe regime (where there is less than one fringe in the image). The method does not require prior knowledge of the fringe phase or fringe contrast, which removes the need for experimental procedures to locate fringe centers and for calibration of the fringe contrast. Our method dramatically advances the robustness of PSI in the signal regime of partial interference fringes.

I. INTRODUCTION

In a rotating frame, an atom interferometer experiences a Sagnac phase shift proportional to the inner product of the rotation vector and the Sagnac area [1]. The Sagnac area is proportional to the atoms' initial velocity in the plane perpendicular to the rotation vector for free-space atom interferometers, such as beam atom interferometers and launched atom interferometers. In beam atom interferometers, the atomic beam has a wide velocity distribution in the longitudinal direction. The signals at low rotation rate have high fringe contrast, whereas at high rotation rates the signals cancel, leading to vanishing fringe contrast [2]. In launched atom interferometers, cold-atom sources are used because they have velocity distribution with a reduced width, and the atoms are launched with an initial velocity in a controllable fashion [3]. For guided atom interferometers, the matter-wave trajectories follow the guide geometry, and the Sagnac area is fixed [4, 5].

Contrary to the above-mentioned conventional atom interferometry techniques, point source atom interferometry (PSI) [6, 7] uses the expansion of a single cold-atom cloud to simultaneously operate many Sagnac interferometers at once, and then maps the signal from each velocity class onto a unique point in the image plane, using the position-velocity correlation of an expanded point source. In the expanding cloud, different velocity classes have different Sagnac areas, all of which contribute to the final interferometer signal. Because of the parallel operation, PSI measures one axis of acceleration, and two axes of rotation from a single cold-atom source and without interleaving measurements. PSI is also distinct from conventional atom interferometer gyroscope techniques because a single rotation measurement with PSI yields a unique reading for the underlying rotation rate.

In PSI, a $\pi/2 - \pi - \pi/2$ Raman pulse sequence is applied to an ensemble of cold atoms as it expands. Assuming the Raman laser beams are counter-propagating along the z -axis, the components of the rotation vector projected onto the xy -plane generate an interferometer phase gradient with the following x and y components,

$$k_x = -\frac{2k_{\text{eff}}T_R^2}{T_{\text{ex}}}\Omega_y \text{ and } k_y = \frac{2k_{\text{eff}}T_R^2}{T_{\text{ex}}}\Omega_x \quad (1)$$

where k_{eff} is the effective wave vector of the Raman laser, Ω_x and Ω_y are the components of the rotation in the xy -plane, T_R is the time between the Raman pulses, T_{ex} is the total expansion time of the cold-atom cloud ($T_{\text{ex}} \geq 2T_R$) [8]. There is no gradient along the z direction in this configuration. This phase gradient results in a sinusoidal fringe pattern in the population distribution across the final cloud. In principle, the rotation rate can be extracted from a single fringe image, but a clockwise and counter-clockwise rotations remain indistinguishable. The rotation direction can be determined by taking a series of fringe images while scanning the Raman laser phase and observing the direction of the fringe travel. The acceleration along the Raman beam direction and the Raman laser phase determine the phase of the fringes in the image.

Because PSI fringe images are essentially windowed pictures of monochromatic plane waves, it is intuitive to use parametric fitting to extract the fringe contrast, orientation, frequency, and phase, where the latter three parameters can be converted to rotation and acceleration readings. However, parametric fitting to a fraction of a fringe that has an unknown phase is challenging because, in practice, the plane wave is usually damped with a Gaussian envelope due to spatial variation of atomic distribution or contrast, plus other noises exist in the images. Since the phase gradient (and thus the number of fringes) is proportional to the rotation rate, a lower rotation rate that generates less than one fringe can only be measured with significant error, except when the signal-

* yunjhih.chen@colorado.edu

to-noise ratio is excellent.

Dickerson *et al.* have described this problem of measuring small rotations in the partial-fringe regime when they measured the Earth's rotation [6]. In their work, they applied a counter-rotation that nulls the phase gradient and thereby yields the Earth rotation rate. Instead of parametric fitting the entire cold-atom image to obtain the phase gradient as they scanned the counter-rotation, they detected the differential phase between the left-half and right-half of a cold-atom cloud with an ellipse fitting procedure [9].

However, the approach in [6] may be sensitive to fluctuations in the atomic density distribution. This concern is mentioned in the work by Sugabaker *et al.* where the authors used a different approach and demonstrated gyrocompassing [7]. In that study, an experimental phase shear, in the form of Raman laser beam-tilt for the third Raman pulse, is applied to the cold-atom cloud to increase the number of fringes across the cloud to about 2.5 so that their parametric fitting procedure is operational.

We propose a different approach – instead of analyzing the fringe images, we convert the fringes in the population distribution into an interferometric phase map [8], which allows a direct analysis of the phase gradients and the acceleration phase, regardless of the number of fringes. This is accomplished by an experimental method that convert four fringe images into a phase map. We have termed the method “Simple, High dynamic range, and Efficient Extraction of Phase map”, or “SHEEP.” The SHEEP method does not loose sensitivity in the partial fringe regime.

As we are going to demonstrate in the following sections, the SHEEP method returns robust rotation readings and is independent of the fringe phase or the number of fringes in the image, because the analysis is in the phase map domain. The SHEEP method does not require additional experimental means, such as compensation rotation or additional Raman beam tilt, to perform well at low rotations. Further, the SHEEP method does not require a calibration of the fringe contrast. These features add up to unparalleled robustness and efficiency that makes the SHEEP method advantageous for real-time portable applications.

II. THEORETICAL BACKGROUND

A. Extraction of the phase map

Figure 1 describes the concept of the SHEEP method which is to convert four fringe images into a phase map. This conversion is essentially an inverse tangent function of a series of four fringe images, in which the phase of each fringe image differs from the previous one by $\pi/2$ [8, 10]. Experimentally, the stepping of the fringe phase by $\pi/2$ is done by increasing the Raman laser frequency chirp rate by $1/4T_R^2$ each time a new image is taken, with T_R the

time between the Raman laser pulses. Prior knowledge of fringe contrast, orientation, frequency, or phase is not needed (to measure the rotation components Ω_x and Ω_y).

We label the four population ratio images as P_1 , P_2 , P_3 , and P_4 . The pixel value in each image is nominally described by a sinusoidal function of the phase,

$$P_L(x_i, y_j) = \frac{1}{2} [1 - c(x_i, y_j) \cos(\phi(x_i, y_j) + 2\pi\Delta\alpha_L T_R^2)], \quad (2)$$

where $L = 1, 2, 3$, or 4 is the image number, (x_i, y_j) labels the pixel in the i th column and j th row, $c(x_i, y_j)$ is the contrast of the pixel (x_i, y_j) and is not assumed to be constant, $\phi(x_i, y_j) = \phi_\Omega(x_i, y_j) + \phi_a + \phi_l$ is the phase map that contains the rotation phase $\phi_\Omega(x_i, y_j)$, acceleration phase ϕ_a , and the Raman laser phase ϕ_l , and $\Delta\alpha_L$ is the difference in the Raman laser chirp rate from α_0 in image L . α_0 is the Raman laser chirp rate that compensates for the Doppler shift due to the free fall of the atoms. Without loss of generality, we assume $\Delta\alpha_1 = 0$.

We step the chirp rate such that $(\Delta\alpha_{L+1} - \Delta\alpha_L) \times 2\pi T_R^2 = \pi/2$ and calculate the phase map as

$$\phi(x_i, y_j) = \tan^{-1} \left[\frac{P_2(x_i, y_j) - P_4(x_i, y_j)}{P_3(x_i, y_j) - P_1(x_i, y_j)} \right] + n\pi, \quad (3)$$

where n is an integer that removes discontinuities in the phase map. The mathematical form in Equation 3 is similar to the phase-shifting interferometry used in optical interferometry [11–13].

The contrast of each pixel $c(x_i, y_j)$ is a common factor of the numerator and denominator in the argument of the inverse tangent and cancels out in the calculation. Thus, the phase map is separated from the spatial distributions of atoms and the Raman laser Rabi frequency. In other words, the phase of each pixel in the phase map is computed from the pixel's own amplitudes as it steps through a full π oscillation. This operation is independent from the value of neighboring pixels, and thus, in principle, robust against the background structure of the image.

By definition, the output range of the inverse tangent is between $-\pi/2$ and $\pi/2$, resulting in discontinuities in the phase map when the rotation rate is high enough that multiple fringes are created across the cloud. Unwrapping the inverse tangent output, i.e., determining the value of n in Equation 3, does not change the gradient. We note that the value of n changes the global offset of the entire phase map in steps of π , arising from the fact that the acceleration measurement in PSI is fundamentally ambiguous over phase multiples of π as in conventional atom interferometers. Additional techniques can be implemented to resolve the ambiguity problem, especially important for portable applications [14–16].

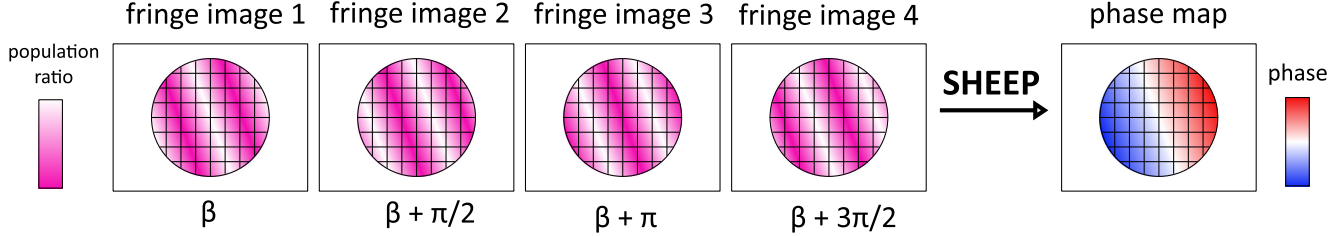


FIG. 1. SHEEP method converts four fringe images into a phase map. In the illustration, β is an unknown fringe phase due to the acceleration phase and the Raman laser phase. The SHEEP method takes a series of four images, and each fringe image's phase differs from the previous one by $\pi/2$. Experimentally, this $\pi/2$ phase stepping is achieved by stepping the Raman laser chirp rate. The SHEEP method returns the phase map, which contains the values of the phase β and the rotation phase gradient. The operation is independent of the fringe contrast, fringe orientation, fringe frequency, or fringe phase.

B. Phase map analysis versus fringe image analysis

The experimentally obtained phase map $f(x, y)$ can be described by a simple linear model with only three fitting parameters, such as:

$$f(x, y) = k_x x + k_y y + \phi_0, \quad (4)$$

where ϕ_0 is the sum of the acceleration phase and the Raman laser phase, k_x is the rotation phase gradient in the x -axis, and k_y is the rotation phase gradient in the y -axis. All three parameters are useful in inertial sensing. The rotation components are recovered from the phase gradients via the relations in Equation 1. The acceleration in z -axis, a_z , can be recovered by the relation $a_z = \phi_0/(k_{\text{eff}} T_R^2)$, but this is not an emphasis in the present work.

The experimentally obtained fringe images can be modeled as a plane wave that has five fitting parameters, such as:

$$g(x, y) = c \cos(k_x x + k_y y + \phi_0) + g_0, \quad (5)$$

where the additional fitting parameters are c , contrast of the fringes (assumed to be constant over the range of the cold-atom cloud), and g_0 , the overall background. If the Gaussian envelope can not be removed by a normalized detection scheme, the fringe images may be modeled by including an additional Gaussian envelope, though at the cost of requiring more fitting parameters.

The phase gradients, the contrast, and the fringe phase are all fitting parameters in the sinusoidal function. In principle, the fitting procedure should not require prior knowledge to return reasonable values of the parameters. However, experimentally, parametric fitting of the fringe images with sinusoidal functions is not as robust as linear fitting of phase maps, as we are going to show in Section IV. We believe that the simplification from sinusoidal fitting with five parameters (fringe analysis) to linear fitting with three parameters (phase map analysis) contributes to the superior robustness of the SHEEP method.

As yet another approach for fringe image analysis, one may consider fast Fourier transform (FFT). In the literature, it is sometimes concluded that FFT is inferior to parametric fitting [17, 18]. FFT-based fringe analysis does not lend itself as a meaningful comparison in our case due to the proximity to the diffraction limit. The size of our experimental images is 1.9×1.9 mm with 36×36 pixels, which corresponds to a k-space resolution of about 3300 rad/m. The rotation phase gradients studied here top out at 6200 rad/m. In the Fourier transform of the images, generally two Fourier peaks are present, with equal phase gradients but on opposite sides of the origin of the Fourier plane. In the partial-fringe regime, these two peaks move close to the plane's origin and interfere with each other in a manner that depends on the acceleration phase and other details, leading to inclusive readings of the phase gradient (without an extensive analysis). The fact that the SHEEP method returns a robust value for the phase gradient that is independent of the acceleration phase is a clear advantage of SHEEP over FFT-based analysis in the partial-fringe regime. The SHEEP method also returns the acceleration phase for free, which is useful for acceleration measurements.

III. EXPERIMENTAL SETUP AND METHODS

The experimental setup has been described in our previous work [19]; however, in the present work, we use a different experimental timing sequence to acquire the four fringe images for demonstrating the SHEEP method (without changing the hardware).

The experiment uses ^{87}Rb atoms laser-cooled in a glass cell with a 1 cm^2 cross-sectional area. At the beginning of each experimental sequence, the atoms are loaded into a six-beam magneto-optical trap (MOT). The cloud of atoms is made smaller and colder with compressed-MOT and molasses stages, resulting in an initial atomic cloud with a diameter of 0.4 mm and a temperature lower than $10 \mu\text{K}$. The freely expanding cloud of atoms is then transferred to the $F = 1, m_F = 0$ sublevel of the ground state

by optical pumping. The Raman $\pi/2 - \pi - \pi/2$ laser pulses are applied in the direction of the local gravitational field. The π -pulse duration is $5 \mu\text{s}$ and the time between pulses is $T_R = 7.8 \text{ ms}$. After the pulse sequence, the cloud is imaged in the plane transverse to the Raman laser beams with state-selective absorption imaging. At the time of imaging $T_{\text{ex}} = 25.9 \text{ ms}$, the cloud has expanded by a factor of 4 and fallen by 3 mm. The total experimental cycle time is 166.7 ms. We performed normalized detection by taking an image of the atoms in the $F = 2$ state, repumping all atoms to $F = 2$, and then taking a second image of the atoms in the $F = 2$ state. The fringe image is obtained by taking the ratio of the first image to the second image and plotting the population ratio of the atoms in $F = 2$ state.

The laser beams that drive the two-photon Raman transitions between the ^{87}Rb $F = 1$ and $F = 2$ states are spatially superimposed with orthogonal circular polarizations. A bias magnetic field is applied in the direction parallel to the laser beams. The laser beam driving the transition from the $F = 1$ state to an intermediate state is denoted as the “F1 beam,” and the other laser beam driving the transition from the $F = 2$ to the intermediate state is denoted as the “F2 beam.” The F1 beam is retro-reflected back to the atoms after passing through the cell, and the polarization is reversed from σ^- -polarization to σ^+ -polarization. The counter-propagating pair of the Raman beams is used to transfer photon momenta to the atoms. The co-propagating pair of Raman beams drives magnetically-sensitive transitions, which are tuned off resonance by the bias magnetic field.

During the Raman interrogation, the frequency of the F1 beam is chirped with a direct digital synthesizer at $\alpha_0 = -25.1 \text{ kHz/ms}$ to compensate for the Doppler shift due to the free fall of the atoms. Varying the chirp rate around α_0 also scans the overall interferometer phase and translates the spatial fringes across the image plane.

Rotation of the lab frame causes the direction of both Raman beams to rotate about the free-falling atoms. We simulate rotation by piezoelectrically sweeping the angle of the retro-reflection mirror of the Raman F1 beam, which causes phase shifts that are equivalent to the shifts caused by a rotation of the lab frame for small mirror rotation angles [20].

IV. EXPERIMENTAL RESULTS

Our objective is to compare the phase map analysis with the more typical fringe analysis by parametric fitting. For the phase map analysis, we extract the phase map with the SHEEP method, then apply a 2D linear fit to the phase map with Equation 4. In the following, we refer to this approach as the “SHEEP method”. For the fringe analysis, we process all four images and then take the average of the results in quadrature since we convert a series of four fringes images into one phase map. We first perform a principal component analysis (PCA) to

the set of four images to remove some background noise, and then apply a 2D curve fit to the four cleaned fringe images with the plane wave function in Equation 5. We refer to this approach as “PCA method,” which has been used in previous PSI works [6, 7, 19]. PCA is model-free, and has been used in different atomic systems to remove noises in the images before analyzing the data with a physics model [21, 22] [23]. It should be noted that the comparison is between one phase map and four fringe images. A sample of the phase map and the fringe images can be found in the Appendix.

A. Azimuthal scans of fixed-magnitude rotation vectors

We simulated the precession of a rotation vector in the plane perpendicular to the Raman laser beams by applying a fixed rotation rate while stepping the direction of the rotation from 0 to 360 degrees in two-degree steps. In each rotation step, we recorded a series of four fringe images with fringe phases of 0, $\pi/2$, π , and $3\pi/2$ to the unknown acceleration phase. We process the sets of four images with the SHEEP method and the PCA method separately, and plot the measured rotation phase gradients versus the azimuthal angle of the applied rotation vector.

The traces obtained by the SHEEP method and the PCA method are shown in Fig. 2. Because the rotation vector rotates about the direction of the Raman laser beams, the x -component of the phase gradient follows a sine curve while the y -component of the phase gradient follows a cosine curve, via the relation in Equation 1.

Qualitatively, the SHEEP method resolves the sinusoidal variation in all three cases, while the PCA method loses sensitivity as the rotation rate becomes smaller.

In Fig. 2 the traces of the PCA method are plotted as the absolute value of the rotation phase gradients because the sign of the phase gradients k_x and k_y returned by the plan wave fitting is meaningless. An extended experimental procedure and additional analysis would be needed to determine the direction of the fringe travel, and thus the sign of the phase gradient. This is not relevant for the sensitivity comparison here; however, the ability of the SHEEP method to distinguish between a rotation and a counter-rotation further highlights its practical advantages.

We notice that there is a non-zero phase gradient offset even when there is no applied rotation rate. These phase gradient offset was slowly changing over the time scale of this work [24]. An example of this phase gradient offset is visible in Fig. 2 (a), where both sinusoidal curves are centered at a non-zero value in the vertical direction.

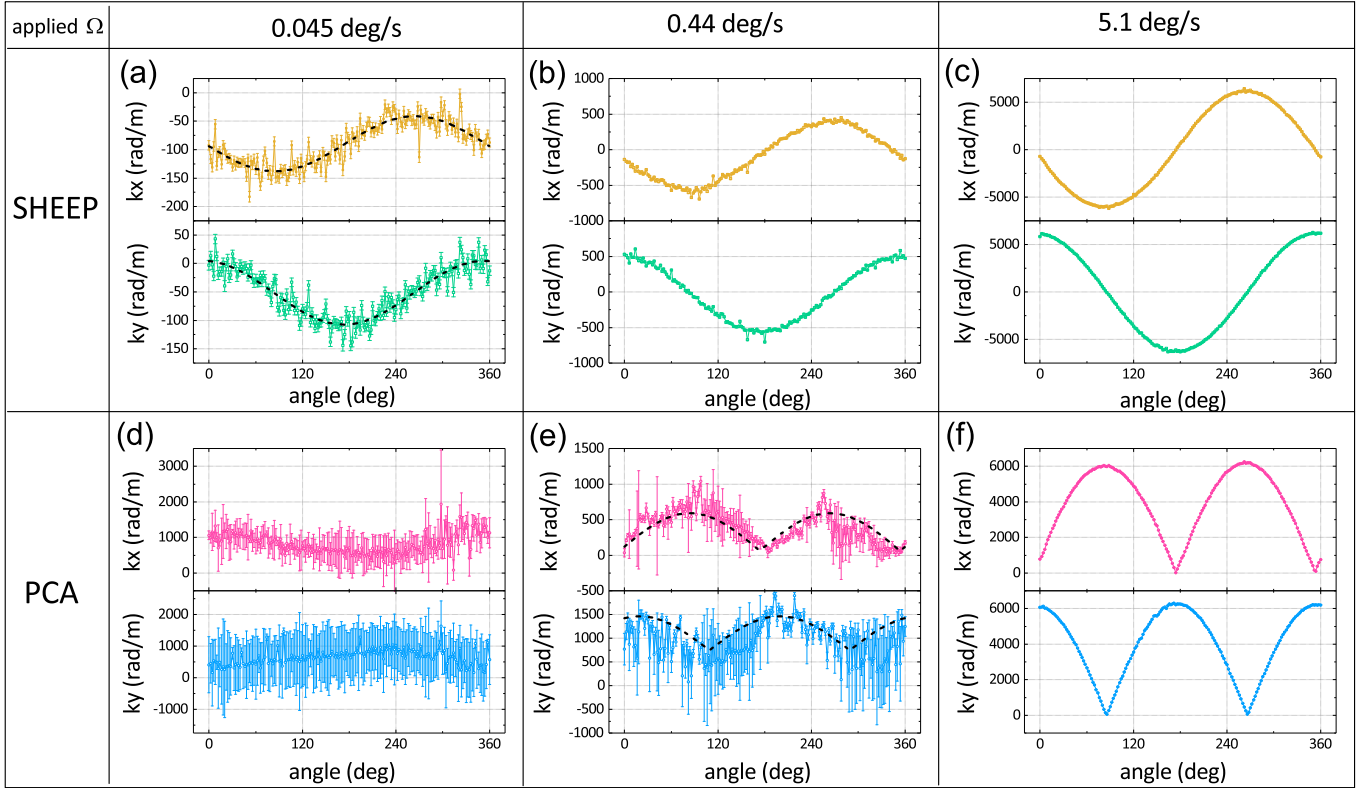


FIG. 2. Traces of simulated precessions from 0 to 360 degrees with the SHEEP method and the PCA method, for the indicated rates. The half length of the error bar attached to each point is the value of the 2D fit error. In (a), the dashed lines are sine and cosine fits to the time traces. In (e), the dashed lines are magnitude-sine and cosine fits. An example of the fringe images for the case of 5.1 deg/s rotation ((c) and (f)) can be found in the Appendix.

B. Statistical error of single cycle rotation measurements

Figure 3 shows the results of single cycle rotation measurements (of a set of four images) returned from the PCA method (pink circles) and the SHEEP method (green squares and purple triangles). Both the measured rotation value and the error in Fig. 3 are normalized to the applied rotation rate. The two methods return similar normalized values and errors when the images have more than one fringe; however, the PCA method worsens immediately after entering the partial-fringe regime, while the normalized value and the error of the SHEEP method remain low down to the lowest rotation rates studied. In other words, the two methods are similar in the multiple-fringe regime; however, in the partial-fringe regime, the PCA method gradually loses its sensitivity. Contrary to the PCA method, the SHEEP method remains robust without any correction and the dynamic range is at least 10 dB better than that of the PCA method. The dynamic range of the SHEEP method is further improved when the phase gradient offset (at zero applied rotation rate) is removed (purple triangles).

For a perfect point source, the normalized rotation should be one, i.e., with a scale factor that equals one.

However, a scale factor is expected to be around 0.9 in this work, because the cold-atom cloud expands by a factor of about four and is therefore not an ideal point source. Avinadav and Yankelev *et al.* have demonstrated methods to correct this effect [25].

The rotation phase gradient, and thus, the number of fringes, scales with the rotation rate and the time between the Raman laser pulses (assuming $T_{\text{ex}} \approx 2T_R$, see Equation 1). In this work, T_R is 7.8 ms due to the small dimension of our experimental setup. We also plot the calculated number of fringes of an ideal point source in Fig. 3 in order to highlight the fact that the measurement covers both multiple-fringe regime and partial fringe regime. Due to the reduced scale factor, the actual number of fringes is slightly lower [8].

C. Allan deviation of rotation measurement at one second

We also record a time series of images where the applied rotation rate and the rotation direction are fixed. We repeat the measurement at a few different applied rotation rates, including zero applied rotation rate. Figure 4 (a) and (b) show two samples of Allan deviation

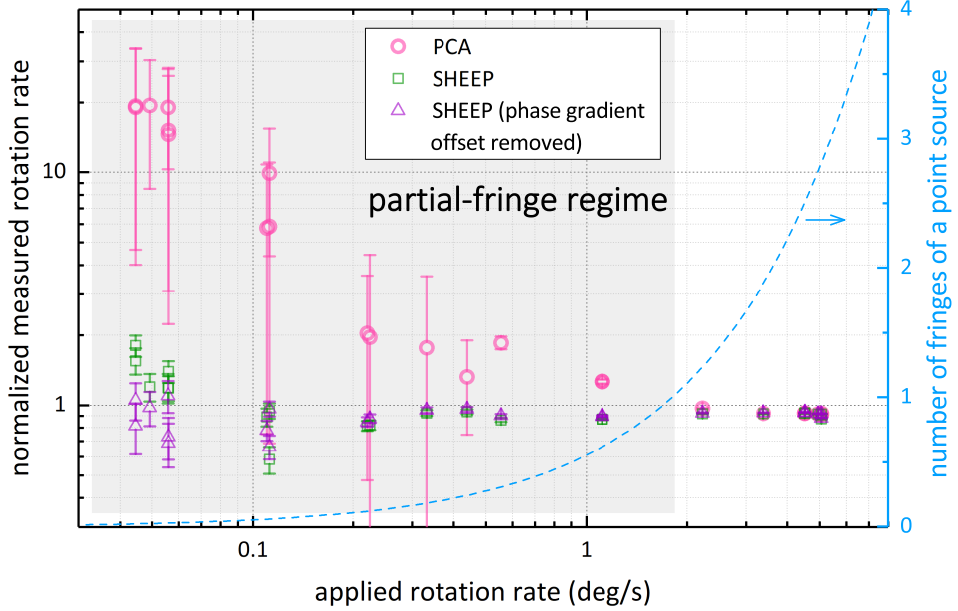


FIG. 3. Fit results from single cycle rotation measurements, in both the SHEEP method and the PCA method, versus the applied rotation rate. The left vertical axis is the measured value returned from the fitting procedure, and is plotted as normalized values. The half length of the error bar is the normalized 2D-fit standard error. The blue dashed line (vertical axis on the right) shows the calculated number of fringes along the diagonal of an image versus rotation rate for a point source with $T_R = 7.8$ ms and $T_{ex} = 25.9$ ms.

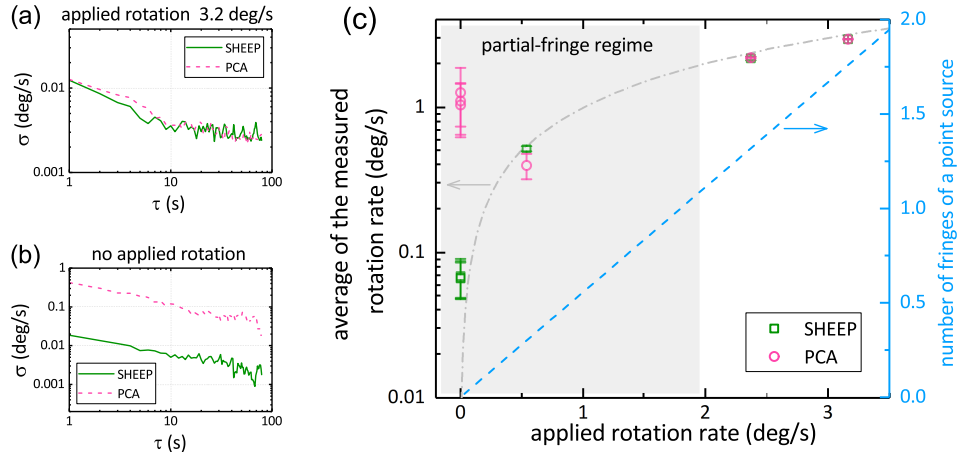


FIG. 4. Allan deviation of rotation measurement. (a) and (b) are plots of the Allan deviation curves of rotation measurements at an applied rotation rate of 3.2 deg/s and zero applied rotation rate, respectively. We fit the curves from 1 to 10 seconds with a function $A/\sqrt(\tau)$, where the fit parameter A is an estimate of the Allan deviation at one second. We plotted the average of the measured rotation rate versus the applied rotation rate in (c) with the half-length of the error bars equals the value of coefficients A . The dot-dashed line equals the applied rate (scale factor of one). The dashed line with the vertical axis on the right shows the number of fringes in the image (calculated in the same manner as described in the caption of Fig. 3).

plots at an applied rotation rate of 3.2 deg/s and zero applied rotation rate, respectively. The Allan deviation curves from the SHEEP method and the PCA method are not significantly different from each other in (a). However, in the case of zero applied rotation rate, shown in (b), the curve for the PCA method is at least a factor of 10 higher while the curve of the SHEEP method remains

at about the same level as in Fig. 4 (a).

Figure 4 (c) shows the mean value of the measured rotation rate. The half-lengths of the error bars attached to each point are the Allan deviations at one second. To guide to eye, in Fig. 4 (c) we also show the applied rotation rate itself with a dot-dashed line. In the multiple-fringe regime, both SHEEP and PCA methods return

similar mean values and Allan deviations at one second. In the partial-fringe regime, the mean values of the PCA method deviate from the dot-dashed line and have larger Allan deviations. At zero applied rotation rate, the mean value of the SHEEP method is not exactly zero, due to the non-zero phase gradient offset discussed in Sec. 2.

From Fig. 4 we conclude again that the SHEEP method is more robust than the PCA method and has a wider dynamic range.

V. DISCUSSION

A. Measurable range of rotation rates

In light-pulse atom interferometry, rotation of the laboratory frame causes \vec{k}_{eff} to rotate such that atoms receive momentum kicks in slightly different directions from the sequential laser pulses, and with the result that atomic spatial wavefunctions at the output of the interferometer do not completely overlap. This walk-off reduces the interferometer contrast at high rotation rates and sets a fundamental upper limit for the maximal rotation rate that can be measured. In our compact instrument, the finite-sized initial cloud and the small expansion factor also reduce the contrast of the spatial fringe pattern as the rotation rate increases [8], which also sets an upper limit on the measurable rotation rate. In Fig. 2, the highest rotation rate of $5.1^{\circ}/\text{s}$ is not limited by the walk-off or fringe contrast but simply by the upper limit of our ability to simulate rotation through the angular motion of the retroreflecting mirror. The lowest rotation rate of $0.045^{\circ}/\text{s}$ is limited by the electronic noises of our piezoelectric actuator electronics of the retroreflecting mirror.

The upper and lower limits on the measurable rotation rates also depend on technical factors such as the resolution of the analog-to-digital converter in the camera, the pixel size, the camera noise, and the system vibration noise. This experiment is built on a floating optical table without active vibration isolation. We use relatively short Raman interrogation time $T_R = 7.8 \text{ ms}$ to avoid the effects of vibration. This short T_R is also compatible with the dimensions of the glass cell used in the experimental setup.

B. Unambiguous rotation measurement

In conventional atom interferometers, the rotation is measured from the rotation phase, which is typically derived from the population ratio via an inverse sinusoidal function. However, the inverse sine is ambiguous by an integer multiple of π , and therefore the measurement does not provide a unique value of the underlying rotation and

In contrast, PSI gives a unique value of the rotation. The interferometer rotation phase depends linearly on the atom velocity v as $\phi_{\Omega} = 2\vec{k}_{\text{eff}} \cdot (\vec{\Omega} \times \vec{v})T_R^2$, so the magnitude of the rotation depends on the quantity

$d\phi_{\Omega}/dv = 2k_{\text{eff}}T_R^2\Omega$. The quantity $d\phi_{\Omega}/dv$ is inherently measured in PSI as a spatial phase gradient across the cold-atom cloud because of the position-velocity correlation of an expanding cloud. The spatial phase gradient is a one-to-one function of the rotation vector projected onto the image plane.

VI. APPLICATIONS

In light of the rotation dynamic range, unambiguity, and robustness provided by the SHEEP method, a PSI instrument may be operated in the free-running mode that returns rotation readings for inertial navigation applications. A PSI instrument may also be operated in a zero-fringe locking, closed-loop [26–28] mode that provides a rotation-free environment for another instrument. In a closed-loop mode, real-time phase maps generated by the SHEEP method are used as a servo input to an actuator that cancels the platform’s rotation. In high-precision atom interferometer gravimeters, sources that generate spatial variation in the population distribution in the final cloud, such as the Earth’s rotation [20], the rotation of a moving platform, or the Raman laser wavefront [29, 30], can cause systematic errors in the acceleration measurement. The SHEEP method, combined with additional tools, may be used to characterize those spatially-dependent systematic effects *in situ*.

VII. CONCLUSIONS

We have demonstrated a new method which we termed “Simple, High dynamic range, and Efficient Extraction of Phase map”, or “SHEEP”. The SHEEP method extracts the phase map of a point-source atom interferometer from four fringe images. We have compared the SHEEP method to a conventional fringe-analysis approach, in which images are processed with principal component analysis and subsequently fitting with parametric functions. We have demonstrated that the two methods are generally equivalent in the multiple-fringe regime (moderate and fast rotations); however, SHEEP is more robust in the partial-fringe regime (slow rotations).

The SHEEP method does not require prior knowledge of the fringe phase, fringe contrast, or the range of the rotation rate. These advantages benefit the experimental design, data acquisition, and analysis procedures in fieldable applications, because they considerably simplify the decision tree in instruments.

ACKNOWLEDGMENTS

We acknowledge valuable contributions from Gregory W. Hoth. We thank Kevin Coakley and Jolene Splett for helpful discussions in statistics. We thank William McGehee for critical comments on our work.

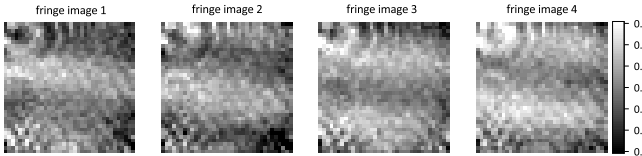


FIG. 5. Fringe images, plotted as population ratio of the $F = 2$ state. The imaging plane is perpendicular to the direction of the Raman laser beams. The fringe phases are $0, \pi/2, \pi$, and $3\pi/2$ relative to the unknown acceleration and Raman laser phase. All images have 36×36 pixels and a physical size of $1.9 \times 1.9 \text{ mm}^2$.

	k_x (rad/m)	k_y (rad/m)	ϕ_0 (rad)
lower	-7000	-7000	-3.14
upper	7000	7000	3.14

TABLE I. Parameter limits for Equation 4 for the SHEEP method.

We thank Christopher Oates and Christopher Holloway for comments on the manuscript. A. H. was supported for this work under an NRC Research Fellowship award at NIST. R. B. was supported by the NIST Guest Researcher Program and the Délégation Générale de l'Armement (DGA). This work was funded by NIST, a U.S. government agency, and it is not subject to copyright.

APPENDIX

Figure 5 shows a set of four experimental fringe images with an applied rotation rate of 5.1 deg/s, which is the highest rotation rate studied in this work. We use a commercial math software and its built-in fitting functions to perform the 2D fit. The fit function uses the trust-region-reflective algorithm and the lower and upper limits of the fitting parameters listed in Tables I and II, for fitting with Equations 4 and 5, respectively.

A. SHEEP

For the SHEEP method, we do not perform any pre-processing on the fringe images. We convert the fringe images into a phase map with Equation 3 and then unwrap the inverse tangent output. We use the pixel value difference in the phase map to compute a set of initial fitting parameters, and then apply a 2D linear fit to the phase map for once. We convert the fit parameter results from this single trial into the measured rotation rate and acceleration phase.

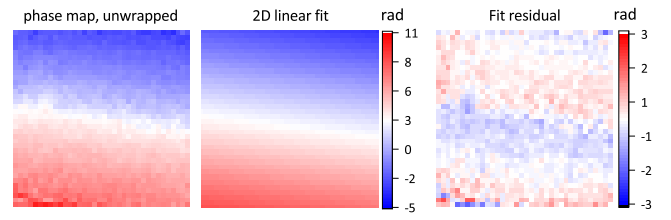


FIG. 6. Sample images of the SHEEP method. Left: phase map derived from the fringe images in Figure 5, with the inverse tangent function output unwrapped. Middle: 2D linear fitting to the phase map with the function in Equation 4. Right: fit residual. All images have 36×36 pixels and a physical size of $1.9 \times 1.9 \text{ mm}^2$.

	k_x (rad/m)	k_y (rad/m)	ϕ_0 (rad)	c	g_0
lower	-7000	-7000	-3.14	0.01	-0.5
upper	7000	7000	3.14	0.99	0.5

TABLE II. Parameter limits for Equation 5 for the PCA method.

B. PCA

For the PCA method, we first process the set of four fringe images with PCA. A mean image is generated as the average of all four images. Each image is centered on this mean image by subtracting the mean image. The principal components of the four centered images are calculated. We use the leading two principal components to reconstruct the images without adding the mean image back to the reconstructed images. The reconstructed images are plotted in the top row of Fig. 7. The background noise is mostly removed in those processed images and the images are ready for 2D sinusoidal fitting.

A 2D sinusoidal fitting function repeatedly fits the same fringe image for 50 times, with newly generated initial fit parameters each time. A uniform random number generator generates initial fit parameters between the upper and lower limits in Table II. We use the optimized fit parameters from the trial that has minimal residual. In this way we approximate a global search of parameters.

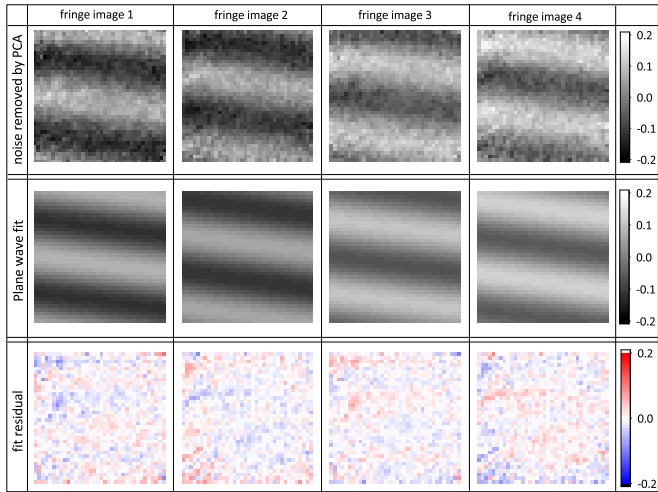


FIG. 7. Sample images of the PCA method. Top row: fringe images reconstructed by PCA. Middle row: 2D fitting to the reconstructed images with the plane wave function in Equation 5. Bottom row: fit residual. All images have 36×36 pixels and a physical size of $1.9 \times 1.9 \text{ mm}^2$.

[1] P. Storey and C. Cohen-Tannoudji, *Journal de Physique II, EDP Sciences* **4**, 1999 (1994).

[2] T. L. Gustavson, P. Bouyer, and M. A. Kasevich, *Phys. Rev. Lett.* **78**, 2046 (1997).

[3] D. Savoie, M. Altorio, B. Fang, L. A. Sidorenkov, R. Geiger, and A. Landragin, *Science Advances* **4** (2018), 10.1126/sciadv.aaau7948.

[4] S. Wu, E. Su, and M. Prentiss, *Phys. Rev. Lett.* **99**, 173201 (2007).

[5] E. R. Moan, R. A. Horne, T. Arporntip, Z. Luo, A. J. Fallon, S. J. Berl, and C. A. Sackett, *Phys. Rev. Lett.* **124**, 120403 (2020).

[6] S. M. Dickerson, J. M. Hogan, A. Sugarbaker, D. M. S. Johnson, and M. A. Kasevich, *Phys. Rev. Lett.* **111**, 083001 (2013).

[7] A. Sugarbaker, S. M. Dickerson, J. M. Hogan, D. M. S. Johnson, and M. A. Kasevich, *Phys. Rev. Lett.* **111**, 113002 (2013).

[8] G. W. Hoth, B. Pelle, S. Riedl, J. Kitching, and E. A. Donley, *App. Phys. Lett.* **109**, 071113 (2016).

[9] G. T. Foster, J. B. Fixler, J. M. McGuirk, and M. A. Kasevich, *Opt. Lett.* **27**, 951 (2002).

[10] G. W. Hoth, *Development and Characterization of an Interferometer Based on an Expanding Ball of Atoms*, Ph.D. thesis, University of Colorado at Boulder (2016).

[11] J. H. Bruning, D. R. Herriott, J. E. Gallagher, D. P. Rosenfeld, A. D. White, and D. J. Brangaccio, *Appl. Opt.* **13**, 2693 (1974).

[12] E. P. Goodwin and J. C. Wyant, in *Field Guide to Interferometric Optical Testing* (SPIE, 2006).

[13] H. Schreiber and J. H. Bruning, in *Optical Shop Testing*, edited by D. Malacara (John Wiley & Sons, Hoboken, 2007).

[14] C. Freier, M. Hauth, V. Schkolnik, B. Leykauf, M. Schilling, H. Wziontek, H.-G. Scherneck, J. Müller, and A. Peters, *Journal of Physics: Conference Series* **723**, 012050 (2016).

[15] Y. Bidel, O. Carraz, R. Charrière, M. Cadoret, N. Zahzam, and A. Bresson, *Applied Physics Letters* **102**, 144107 (2013).

[16] X. Wu, Z. Pagel, B. S. Malek, T. H. Nguyen, F. Zi, D. S. Scheirer, and H. Müller, *Science Advances* **5** (2019), 10.1126/sciadv.aax0800.

[17] Zhaoqiang Bi, Jian Li, and Zheng-She Liu, *IEEE Transactions on Aerospace and Electronic Systems* **35**, 267 (1999).

[18] H. C. So, Kit Wing Chan, Y. T. Chan, and K. C. Ho, *IEEE Transactions on Signal Processing* **53**, 2290 (2005).

[19] Y.-J. Chen, A. Hansen, G. W. Hoth, E. Ivanov, B. Pelle, J. Kitching, and E. A. Donley, *Phys. Rev. Applied* **12**, 014019 (2019).

[20] S.-Y. Lan, P.-C. Kuan, B. Estey, P. Haslinger, and H. Müller, *Phys. Rev. Lett.* **108**, 090402 (2012).

[21] S. R. Segal, Q. Diot, E. A. Cornell, A. A. Zozulya, and D. Z. Anderson, *Phys. Rev. A* **81**, 053601 (2010).

[22] R. Dubessy, C. D. Rossi, T. Badr, L. Longchambon, and H. Perrin, *New Journal of Physics* **16**, 122001 (2014).

[23] We noted that there are other widely-used model-free noise-removal techniques, such as the one demonstrated in [31]. However, considering the overall laser excitation and probing scheme used in our work (that the background noise does not just come from one probe laser beam), and the moving nature of the interferometric fringe patterns, PCA is more appropriate for our application.

[24] The non-zero, slow-varying phase gradient offset may arise from some technical sources, such as the Raman laser beam waveform not being uniform.

- [25] C. Avinadav, D. Yankelev, M. Shuker, N. Davidson, and O. Firstenberg, “Rotation sensing with improved stability using point source atom interferometry,” (2020), [arXiv:2002.08369 \[physics.atom-ph\]](https://arxiv.org/abs/2002.08369).
- [26] P. Cheinet, F. Pereira Dos Santos, T. Petelski, J. Le Gouët, J. Kim, K. Therkildsen, A. Clairon, and A. Landragin, [Appl. Phys. B **84**, 643 \(2006\)](https://doi.org/10.1016/j.applphysb.2006.03.017).
- [27] X.-C. Duan, M.-K. Zhou, D.-K. Mao, H.-B. Yao, X.-B. Deng, J. Luo, and Z.-K. Hu, [Phys. Rev. A **90**, 023617 \(2014\)](https://doi.org/10.1103/PhysRevA.90.023617).
- [28] T. L. Gustavson, A. Landragin, and M. A. Kasevich, [Classical and Quantum Gravity **17**, 2385 \(2000\)](https://doi.org/10.1088/0264-9381/17/12/2385).
- [29] V. Schkolnik, B. Leykauf, M. Hauth, C. Freier, and A. Peters, [Appl. Phys. B **120**, 311 \(2015\)](https://doi.org/10.1007/s00340-015-6000-0).
- [30] A. Trimeche, M. Langlois, S. Merlet, and F. Pereira Dos Santos, [Phys. Rev. Applied **7**, 034016 \(2017\)](https://doi.org/10.1103/PhysRevApplied.7.034016).
- [31] C. F. Ockeloen, A. F. Tauschinsky, R. J. C. Spreeuw, and S. Whitlock, [Phys. Rev. A **82**, 061606 \(2010\)](https://doi.org/10.1103/PhysRevA.82.061606).